Surface Structure of Single-Crystal $MoS_2(0002)$ and $Cs/MoS_2(0002)$ by X-ray Photoelectron Diffraction

Ken T. Park, Michelle Richards-Babb,† M. S. Freund, Jeff Weiss, and Kamil Klier*

Zettlemoyer Center for Surface Studies and Department of Chemistry Lehigh University, Bethlehem, Pennsylvania 18015

Received: February 27, 1996[⊗]

The surface structure of a clean $MoS_2(0002)$ and an *in situ* Cs surface-doped $MoS_2(0002)$ has been studied using high-resolution X-ray photoemission spectroscopy. The X-ray photoelectron diffraction (XPD) patterns of the Mo $3d_{5/2}$ and S 2p core levels from a clean, well-ordered $MoS_2(0002)$ show forward focusing intensity maxima along the directions of nearest neighbors in MoS_2 in both the polar and azimuthal angle scans. The XPD patterns in the azimuthal angle scan exhibit a pronounced photoelectron intensity maximum at every 60°, reflecting the 6-fold rotational symmetry of the basal plane. In addition, because of the finite electron escape depth and the short-range order of the scattered photoelectrons, the azimuthal scans of both the Mo $3d_{5/2}$ and the S 2p core levels further display the 3-fold rotational symmetry of the trigonal prismatic local structure, which $MoS_2(0002)$ possesses. The deposition of Cs onto the $MoS_2(0002)$ surface at room temperature did not introduce any significant changes either in the low−energy electron diffraction or in the XPD patterns, indicating the absence of Cs-induced surface relaxation, but a new photoemission was observed 1.6 eV above the valence band edge of MoS_2, which corresponds to the Cs 6s photoelectron shared with the MoS_2 lattice. Thus Cs/MoS_2 represents an electron donor−acceptor (EDA) surface complex.

I. Introduction

Molybdenum disulfide (MoS_2) is of significant interest in many areas in catalysis. Hydrodesulfurization and hydrodenitrogenation are just two active research areas involving MoS_2.[1] More recently, alkali-doped MoS_2 has attracted much attention for its role in direct catalytic synthesis of alcohols from CO and H_2.[2−5] Since the activity and selectivity of a catalyst are greatly dependent upon its surface properties, knowledge of the surface properties is necessary to understand the fundamental relation between structure, electronic states, and reaction dynamics.

Despite the importance of the MoS_2-based catalysts, only a limited number of studies have been published of these catalysts on the interpretation of reaction mechanisms[6−8] as well as on characterization of the alkali-doped MoS_2 surface.[9−12] In an effort to understand the fundamental chemistry involved in the MoS_2-based catalysts, we investigated the surface atomic structures of a clean and Cs-covered $MoS_2(0002)$. The study was carried out using high-resolution X-ray photoemission spectroscopy (HRXPS), where HRXPS routinely achieves an energy resolution better than 0.3 eV and at the same time permits an angle-resolved X-ray photoemission spectroscopy (ARXPS) examination of the system with the purpose of determining surface structure and location of the electrons that are subject to photoemission.

In the recent past, ARXPS has proven to be a powerful surface diagnostic tool rendering short-range local, atomic structure of a surface via directional variation of intensities of the photoemitted electrons,[13,14] in addition to the element-specific and chemical-state-specific electronic information. In particular, for X-ray photoelectrons of kinetic energy above 500 eV, strong intensity maxima are observed along low-index crystallographic axes. The intensity maxima are also known as forward focusing maxima, and they result from the strongly peaked forward scattering amplitude of atoms. The fact that they are the forward projected image of the top few surface layers makes the interpretation of the ARXPS data relatively simple and consequently establishes the ARXPS technique as an effective surface diagnostic tool.[13] ARXPS is especially valuable in our investigation because the use of photoemission from the highly anisotropic, two-element compound MoS_2 promises rich, real space structural information around a particular element and further permits comparisons between different elements occupying nonequivalent emitter sites.

ARXPS also helps determine the interface structure between Cs and MoS_2 with its sensitivity to the short-range order of a surface structure. Although it is known that Cs adsorption at room temperature does not produce any long-range-ordered overlayer structure on the basal plane of MoS_2 based on previous low-energy electron diffraction (LEED) measurements,[9] the possibility of short-range-ordered structure for the Cs overlayer and the effect of adsorbed Cs on the surface structure of the basal plane have not been explored and still remain to be investigated. In addition, the morphology and structure of Cs adatoms on the $MoS_2(0002)$ surface have not been clearly understood. In a study of $Cs/MoS_2(0002)$, Kennou *et al.*[10] reported work function measurements and a temperature desorption spectroscopy (TDS) study and concluded that their results were consistent with agglomeration and clustering of Cs adatoms. A formation of 3D clusters or short-range order within the Cs overlayer should be easily detectable through an X-ray photoelectron diffraction (XPD) pattern of the Cs overlayer or the changes in the substrate XPD patterns upon Cs adsorption. Furthermore, the fact that Cs is a strong scatterer[15] enhances the sensitivity of the ARXPS to the possible short-range-ordered structure of the Cs overlayer.

II. Experimental Part

All the $MoS_2(0002)$ single crystals used in this study were in the form of the natural mineral molybdenite, obtained from

† Present address: Department of Chemistry, West Virginia University, Morgantown, WV 26506.

⊗ Abstract published in *Advance ACS Abstracts,* June 15, 1996.

S0022-3654(96)00586-2 CCC: $12.00

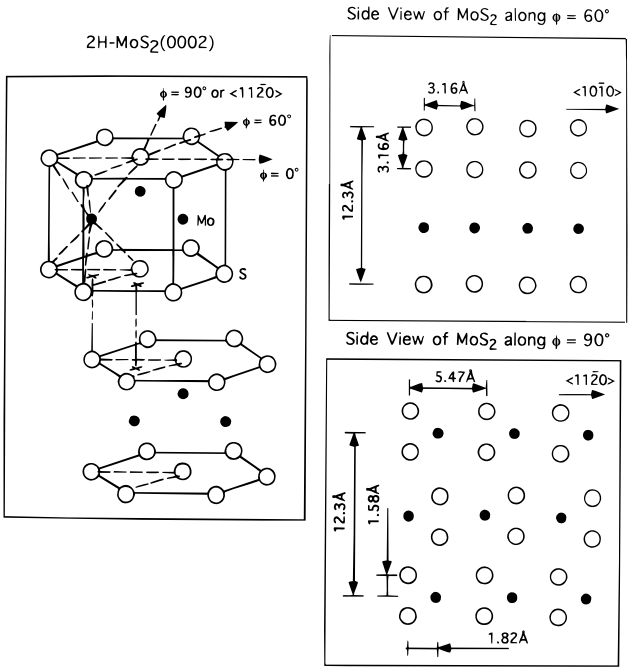

Figure 1. Three-dimensional view of the 2H-MoS_2 structure (left). Also presented are cross-sectional views of a single-crystal MoS_2(0002) surface along $\phi = 60°$ (top right panel) and that along $\phi = 90°$ (bottom right panel).

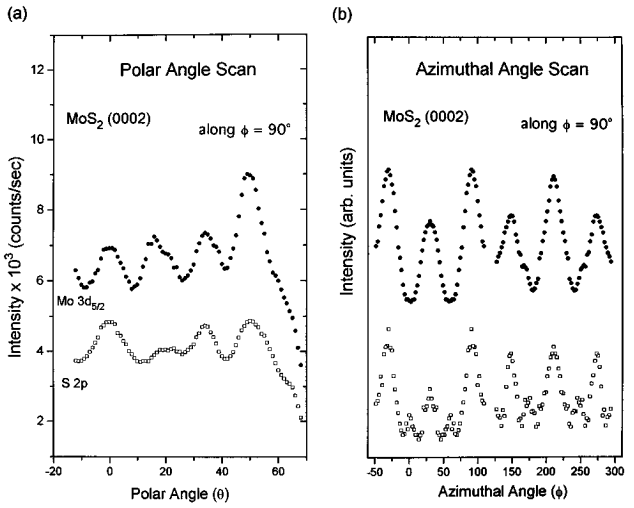

Figure 2. (a) Polar angle scan of the Mo $3d_{5/2}$ (solid circles) and the S 2p (open squares) core level emission along $\phi = 90°$. For all polar angle scans, the sample was rotated with 1° increments such that the angle θ between the surface normal and the direction of the photoelectron emission varied. (b) Azimuthal scan of the Mo $3d_{5/2}$ (solid circles) and the S 2p core (open squares) levels at the fixed polar angle $\theta = 49°$. The sample was rotated about the surface normal with angular increments of 2° in two consecutive runs from $\phi = -50°$ to 110° and from $\phi = 125°$ to 295°. To improve the signal statistics and remove a linear background, data points around $\phi = 30°$ in the first run and $\phi = 210°$ in the second run were folded and averaged.

Ward's Natural Science Establishment. Figure 1 shows the structure of this single-crystal 2H-MoS_2. The two-dimensional MoS_2 sheet belongs to the hexagonal space group (D_{3h}), and locally six sulfur atoms are coordinated to one Mo atom to form the trigonal prismatic structure. The three-dimensional crystal (D_{6h}^5) is formed by stacking the two-dimensional MoS_2 sheets in such a way that two sulfur atoms of the second MoS_2 layer are beneath the Mo of the first layer and the Mo of the second MoS_2 layer is placed under the two sulfur atoms of the first MoS_2 layer. The interaction between two adjacent MoS_2 sheets is of weak van der Waals type, providing a natural cleavage plane of the crystal.

For all samples studied in this experiment, a clean, well-ordered surface of MoS_2(0002) was obtained by the same preparation procedure: peeling off the top surface layers in an inert nitrogen environment. A glovebag was attached to the fast entry chamber of the SCIENTA ESCA[16,17] ultrahigh-vacuum (UHV) system described below. The bag was flushed several times and filled with high-purity nitrogen gas prior to cleaving the sample. A fresh mirror-like surface was exposed inside the N_2-filled glovebag. Then, the sample was immediately mounted on a supporting stub and transferred into the fast entry chamber. To ensure electrical contact, gallium was applied to the edges and the back of the sample. The surface order of the freshly peeled MoS_2 was checked using reverse view LEED optics (Princeton Instrument RVL 8-120). The observed sharp p(1×1) LEED patterns with low background intensity confirmed the cleanliness and the order of the surface. A survey XPS spectrum showed carbon as a minor surface impurity. The carbon impurity is most likely in clustered form, as indicated by the near-perfect LEED pattern.

The experiments were performed using the SCIENTA ESCA-300 HRXPS spectrometer.[16,17] This spectrometer generates high power, monochromatized X-ray flux to excite the photoelectrons. The photoelectrons were collected by a 300 mm mean radius hemispherical electron energy analyzer. The MoS_2 sample was mounted on a manipulator which allowed 3° of translational motion as well as 2° of rotational motion of the sample. The nearest Mo−S bonding direction (along $\langle 11\bar{2}0\rangle$, see Figure 1) was then aligned to the axis of the front column of the electron energy analyzer using the LEED pattern and the strong forward focusing peak of the Mo $3d_{5/2}$ core level. In ARXPS experiments for the Mo $3d_{5/2}$ and S 2p core levels, the sample is rotated while the HRXPS spectrometer is fixed. Detailed information of the spectrometer and the ARXPS geometry of the UHV system in the SCIENTA ESCA laboratory can be found elsewhere.[16] A similar procedure for obtaining a clean, well-ordered MoS_2(0002) surface was also applied to the second MoS_2 single crystal used in the Cs/MoS_2 experiment. After the characterization of the single-crystal MoS_2(0002) surface, Cs was evaporated onto the basal plane of MoS_2 at room temperature from a resistively heated, commercially available SAES getter source[18] The Cs exposure time was gradually incremented by 3 min until the Cs coverage showed saturation after 24 min of total Cs exposure time. During the period of the experiment, the base pressure in the analysis chamber was in the 10^{-10} Torr range.

III. Results

A. ARXPS of Bare MoS_2. The angular variation of both Mo $3d_{5/2}$ and S 2p core level intensities from a clean MoS_2-(0002) surface was investigated (Figure 2). The polar angle scan of the Mo $3d_{5/2}$ core level along $\langle 11\bar{2}0\rangle$ (or $\phi = 90°$) showed four pronounced intensity maxima near $\theta = 0°$, 16°, 34°, and 49° (Figure 2(a)). The peak at $\theta = 49°$ was the most intense one, and its intensity was roughly twice as large as that of the other three peaks. The peak near $\theta = 16°$ displayed a distinctive shoulder near $\theta = 20°$. The peak near $\theta = 34°$ also showed a similar shoulder toward a higher polar angle ($\theta \approx 37°$) but was much less visible. The intensity maxima were quite narrow with a full width at half maximum (fwhm) of *ca.* 9°, with a large anisotropy factor $A = (I_{max} - I_{min})/I_{min} \approx 49\%$. The polar scan of the S 2p core level along $\phi = 90°$ also exhibited four major intensity maxima near $\theta = 0°$, 21°, 34°, and 49°. However, the intensity maximum at $\theta = 49°$ in the polar scan of the S 2p core level was no longer the most dominant peak, unlike that in the polar scan of the Mo $3d_{5/2}$ core level. In

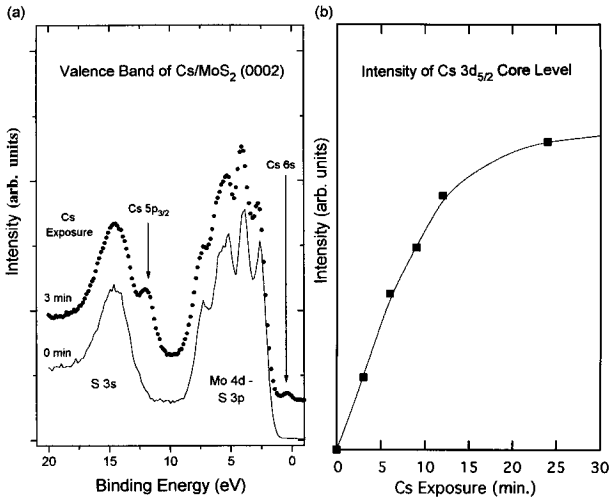

Figure 3. (a) Changes in the valence band spectrum taken at $\theta = 60°$ during the formation of the Cs overlayer on the $MoS_2(0002)$ surface after 3 min Cs exposure (bare MoS_2, line; Cs/MoS_2, solid circles). (b) Intensity of the Cs $3d_{5/2}$ core level as a function of increasing Cs exposure time.

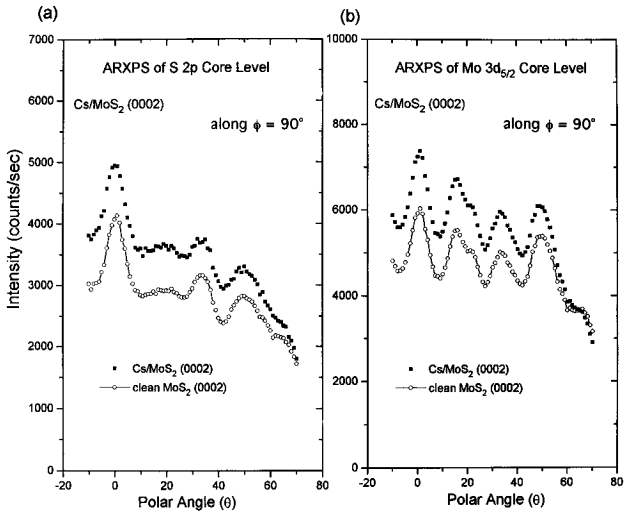

Figure 4. Effect of Cs evaporation at room temperature on the ARXPS of (a) the S 2p and (b) the Mo $3d_{5/2}$ core levels along $\langle 11\bar{2}0 \rangle$ from the $MoS_2(0002)$ surface before (open circles with line) and after 3 min of Cs evaporation (solid squares).

addition, the peak near $\theta = 21°$ was very weak and broad, in contrast to the corresponding peak in the polar scan of the Mo $3d_{5/2}$ core level. The azimuthal angle scan of the Mo $3d_{5/2}$ and S 2p core levels at the fixed polar angle $\theta = 49°$ is presented in Figure 2b. Both core level XPDs showed large intensity maxima at every 60° interval (along $\phi = -30°$, 30°, 90°, 150°, 210°, and 270°), of which the azimuthal scans of the Mo $3d_{5/2}$ and the S 2p core levels further displayed stronger intensity maxima 120° apart at $\phi = -30°$, 90°, and 210°.

B. Core Level ARXPS and Valence Band XPS of Cs/MoS_2. The first 3 min of Cs evaporation on a clean $MoS_2(0002)$ surface introduced the Cs 5p emission line, partly overlapped with the S 3s level of MoS_2, as well as a new density of states at 1.25 eV above the top of the valence band (Figure 3a). We initially assign this new peak as the Cs 6s level since the position of this new valence state was near the Cs 6s valence level position reported in a previous UPS study.[19] Upon 3 min of Cs evaporation, the fwhm of the Mo $3d_{5/2}$ core level increased from 0.39 to 0.51 eV with a slight shift in the peak position toward higher binding energy by 0.07 eV. Similar peak broadening and shifts were also observed in all other electronic levels including the S 2p core level and the valence levels. The steady increase in the Cs exposure time resulted in the increase in the photoemission intensity from various Cs electronic levels including the Cs $3d_{5/2}$ level up to 24 min of total Cs exposure time (Figure 3b). The peak positions of the Cs $3d_{5/2}$ core level were found at BE = 726.0 + 0.3 eV, well within the range of the reported peak positions for cesium metal.[20] From the comparison between the intensity of the Cs $3d_{5/2}$ peak after 3 and 24 min of exposure, the coverage of the adsorbed Cs after 3 min was determined to be about one-fourth of the Cs saturation coverage (Figure 3b).

In contrast, the ARXPS data of the Mo $3d_{5/2}$ and the S 2p core levels before and after 3 min Cs exposure exhibited intensity anisotropy essentially identical to that before Cs adsorption (Figure 4a,b). The Cs evaporation on the basal plane of MoS_2 neither resulted in any new Cs-induced diffraction peaks nor altered the existing intensity maxima. Similarly, the LEED pattern of the Cs-covered $MoS_2(0002)$ surface did not show any significant change in the $p(1\times1)$ LEED pattern of the substrate except for a slight increase in the background intensity.

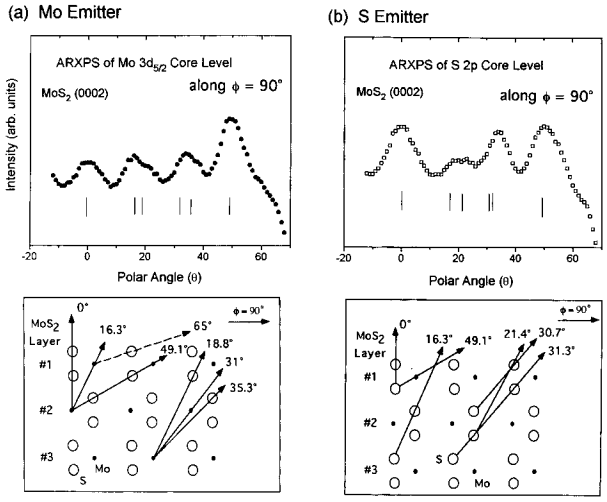

Figure 5. (a) Comparison between the positions of intensity maxima observed in the polar angle scan for the Mo $3d_{5/2}$ core level (upper panel) and the directions along internuclear axes joining Mo emitters and their neighbors in the cross-sectional plane along $\phi = 90°$ (lower panel). (b) The same for the S 2p core level polar scan. Forward focusing directions based on atomic geometry are indicated by vertical bars in the upper panels.

IV. Discussion

A. The Structure of Clean $MoS_2(0002)$ *via* XPD. The intensity maxima in the polar angle scan for the Mo $3d_{5/2}$ and S 2p core levels (Figure 2, parts a and b, respectively) show a good correlation between their positions and the local atomic structure surrounding a particular photoemitter (Figure 5). For the Mo 3d photoemission, the positions of intensity maxima at $\theta = 0°$ and 49° are in excellent agreement with the directions along the internuclear chains joining a Mo emitter and its nearest and next nearest neighbors overlying in the cross-sectional plane along $\phi = 90°$ (Figure 5a). The peak positions of the doublet near $\theta = 16°$ are also observed along the directions joining Mo emitters in layer 2 and 3 to more distant neighbors (at $\theta =$ 16.3° and 18.8°). Likewise, the positions of the intensity maximum near $\theta = 34°$ and its shoulder can be traced to their geometric correspondence between a Mo emitter and its distant neighbors. Figure 5b also shows good agreement between the measured positions of the intensity maxima in the polar scan of the S 2p core level and the local atomic structure around a S emitter. The correlation between the positions of the intensity

maxima and the atomic structure of MoS_2 suggests that the intensity anisotropy observed in the polar angle scan mainly originates from forward focusing,[13] where the photoelectrons from an emitter are focused by neighboring atoms into the forward direction, producing an intensity maximum.

For a more quantitative understanding of the intensity maxima observed in the polar scan, XPD was simulated using a single scattering cluster (SSC) model.[14] In the SSC model within the plane wave approximation, the intensity of photoelectrons can be written as

$$I_{\mathrm{xpd}} \propto \int \mathrm{d}\hat{\epsilon}|(\hat{\epsilon}\cdot\hat{k})\mathrm{e}^{-L/2\lambda} + \sum_j \frac{\hat{\epsilon}\cdot\hat{r}_j}{r_j}\mathrm{e}^{-L_j/2\lambda}|f_j(\theta_j)|W_j \exp(\mathrm{i}\{kr_j(1-\cos\theta_j)+\phi_j(\theta_j)\})|^2 \quad (1)$$

where $\hat{\epsilon}$, $\hat{k}$, and $\hat{r}_j$ are the unit vectors for the polarization, electron emission, and the jth scatterer position, respectively. $|f_j(\theta^j)|$ and $\phi_j(\theta_j)$ are the atomic scattering amplitude and phase for the plane wave[21] incident upon the jth scatterer. The intensity attenuation of the primary and the scattered photoelectron wave amplitudes due to inelastic scattering in the solid was represented by exponential decay terms $\exp(-L/2\lambda)$ and $\exp(-L_j/2\lambda)$, where L and L_j are the distances over which the primary and the scattered waves attenuate. For the inelastic electron mean free path λ in MoS_2, approximately half of the calculated value[22] (17 Å for both the Mo 3d and S 2p photoelectrons) was used in order to take into account the defocusing effect due to multiple scattering.[23,24] The temperature dependence of the XPD due to the vibration of atoms or molecules originates from the Debye−Waller factor W_j. However, for the present study performed at constant room temperature, the Debye−Waller factor was set equal to unity for simplicity. The property of the unpolarized X-ray beam was simulated by calculating the intensities for two orthogonal polarization directions: one in the plane of the incident X-ray beam and the photoemitted electrons and the other perpendicular to the plane of the scattering event. The photoemission intensity was calculated and subsequently averaged over the two polarization directions. Each data point in the calculated XPD spectrum was further averaged to simulate angle-averaging due to the finite acceptance cone of the photoelectron detector ($\Delta\theta \approx 4°$). The scattering cluster for simulation was generated by stacking up two-dimensional MoS_2 layers. The two-dimensional MoS_2 layer in the shape of a parallelogram contained a total of 49 MoS_2 molecules, and the dimensions of the sheet are seven MoS_2 units long in the directions of each surface Bravais lattice vectors $\vec{a}$ and $\vec{b}$.

The calculated polar angle dependence of the Mo $3d_{5/2}$ core electrons in $MoS_2(0002)$ is presented in Figure 6 for up to four MoS_2 layers considered. For a single MoS_2 sheet as an emitting layer (bottom curve of Figure 6), the SSC calculation produces a peak at $\theta = 65°$ resulting from forward scattering of Mo photoelectrons by the top sulfur atom of the adjacent MoS_2 unit (dashed line in Figure 5a). When an additional MoS_2 layer is added (the second curve from the bottom of Figure 6), the SSC calculation predicts two strong forward focusing maxima at 0° and 49°, which correspond to the two directions along the nearest and the next nearest neighbors for the Mo emitter in the second MoS_2 layer. In addition to these intense peaks, two weak intensity maxima also appear near 17° and 28°. The peak near 17° originates from forward focusing of the electrons from layer 2 by the Mo scatterer in layer 1 (Figure 5a). On the other hand, the peak near 28° is the first-order diffraction peak from the strong forward focusing maximum at 49°. For four MoS_2 layers as an emitting layer, an intensity maximum emerges near

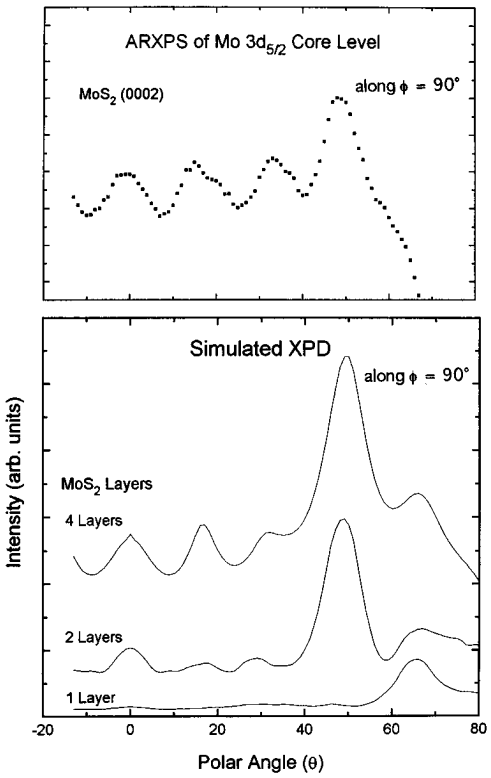

Figure 6. Comparison between the polar angle scan of the Mo $3d_{5/2}$ core level along $\phi = 90°$ (top panel) and the calculated XPD patterns in various MoS_2 layers (bottom panel), using the single scattering cluster (SSC) model.

32°, which is the forward focusing maximum resulting from the Mo $3d_{5/2}$ core electrons in layer 3 scattered by the Mo atoms in layer 2 (Figure 5a). As more MoS_2 layers are added, the SSC calculation successfully reproduces all the major forward focusing maxima observed in experiment. It is also noted that the increased number of MoS_2 layers decreases the peak intensity at 65°, predicted by theory in comparison with other maxima and consequently yields a better agreement with the observed intensity anisotropy in experiment.

The SSC calculation also reproduces the experimentally observed 3-fold rotational symmetry in the azimuthal angle scan (Figure 7a). For both the Mo $3d_{5/2}$ and the S 2p emission, the SSC successfully produces the forward focusing maxima with the 3-fold symmetry in the same orientation observed in experiment: stronger intensity maxima are found along $\phi = -30°$, 90°, and 210°, while the weaker ones are along $\phi = 30°$, 150°, and 270° (experiment, full circles for Mo and open squares for S; SSC calculation, dashed and solid lines for Mo and S, respectively). The SSC calculation also reproduces the small satellite features observed in the S 2p azimuthal scan at 0°, 60°, 120°, 180°, 240°, and 300° with 60° intervals (Figure 2b). These minor peaks of the 6-fold symmetry directly result from forward focusing by sulfur atoms near $\theta = 45°$ along $\{10\bar{1}0\}$ directions (see Figure 1), which substantially contributes to the photoelectron intensity collected at $\theta = 49°$.

The 3-fold rotational symmetry observed in the azimuthal angle scan has the following significance in our ARXPS measurements on the basal plane of MoS_2. First, the observation was only possible because forward focusing is a short-range, real space mapping of local atomic structure with a finite, yet surface-sensitive depth profile unlike LEED. Second, it was essential that the cleaved surface of $MoS_2(0002)$ was atomically smooth and composed mainly of a single basal plane. From the MoS_2 structure, it is seen that the orientation of the MoS_2 units in each sheet alternates as one moves from one MoS_2 sheet to an adjacent one (see Figure 1). Therefore, if the surface had

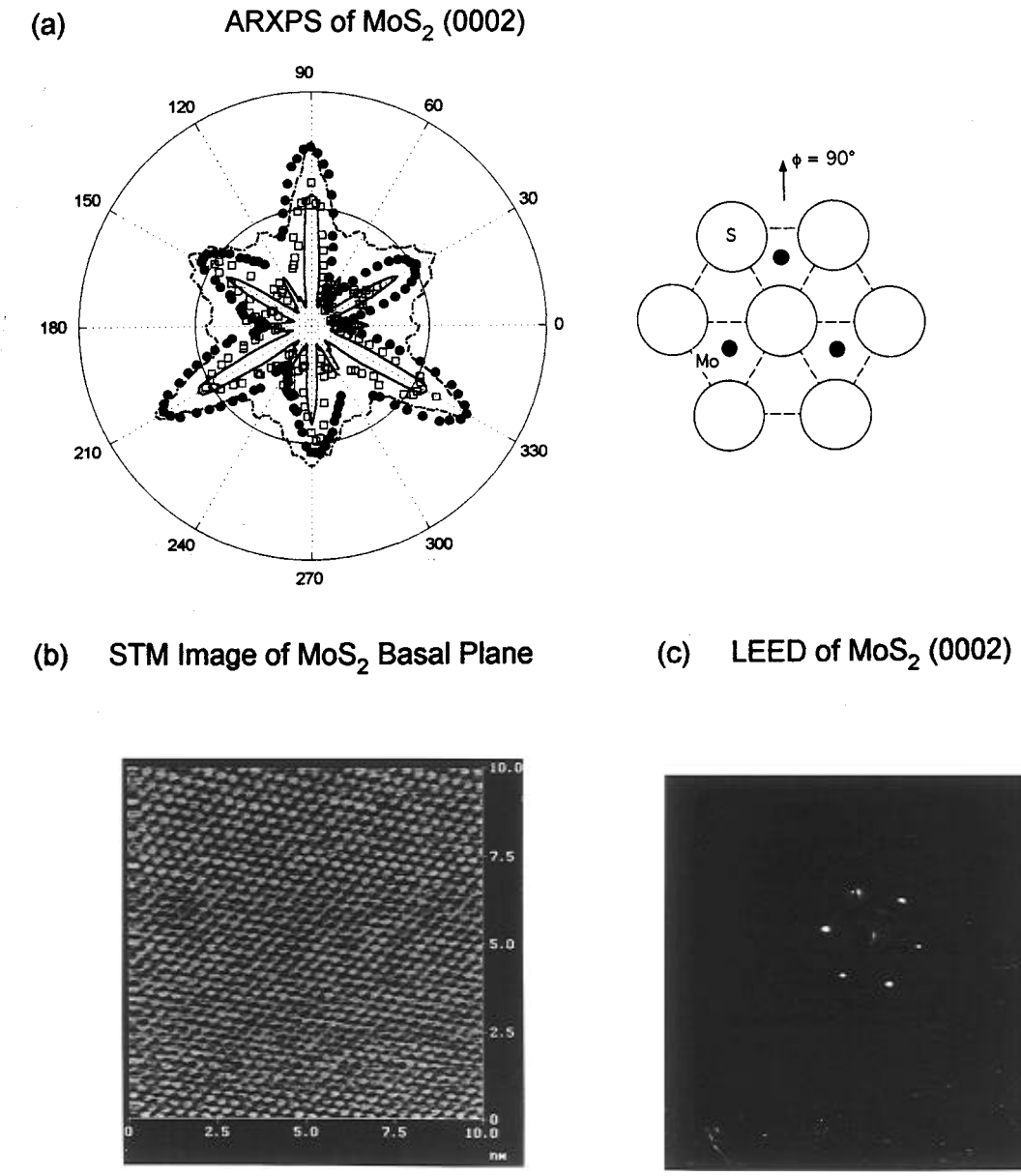

Figure 7. (a) Azimuthal scans for the Mo $3d_{5/2}$ and the S 2p core levels depicting the 3-fold rotational local symmetry of MoS_2(0002) (right). The experimental data for the Mo $3d_{5/2}$ and the S 2p core levels are displayed as solid circles and open squares, respectively. Also shown are the calculated azimuthal angle scans using SSC for the Mo $3d_{5/2}$ (dashed line) and the S 2p (solid line) core levels. (b) STM image of a clean MoS_2(0002) surface in air (10 nm × 10 nm). (c) LEED pattern obtained from the same clean MoS_2(0002) surface used in the present ARXPS experiment.

a large number of random steps and terraces in atomic scale, the surface would contain a more or less equal number of MoS_2 units pointing in both $\phi = 90°$ and $-90°$ directions, producing the 6-fold rotational symmetry instead of the 3-fold symmetry. The flatness in atomic scale on a MoS_2(0002) single-crystal surface was further supported by the STM image (Figure 7b). A similarly prepared single-crystal MoS_2(0002) shows an atomically smooth single basal plane of hexagonal symmetry even in air, as has been observed in many other laboratories.[25,26] However, XPD provides an easy and straightforward means of determining the orientation of the buried Mo triangles in the basal plane on a scale determined by the area of the X-ray beam, 1 × 2 mm. This is the same surface that exhibited the 6-fold symmetry of the Bravais lattice in reciprocal space (Figure 7c).

B. The Structure of Cs/MoS_2(0002) and Electronic Changes in the Valence Band. Our recent investigation of the valence band structure on Cs/MoS_2(0002) using ARXPS[27] indicated that the new density of states above the top of the valence band is a signature of delocalized Cs 6s electrons into the MoS_2 conduction band. Calculations using the solid state extended Hückel theory for Cs/MoS_2 further suggested a large degree of delocalization of the Cs 6s electron and about 90% of charge transfer from the Cs atom to the substrate. The charge transfer from Cs to the substrate is consistent with a dipole formation at low Cs coverages, consistent with a large Cs desorption activation energy of $E_a = 64$ kcal/mol reported in the previous study of Cs/MoS_2 by Kennou *et al.*,[10] a much larger value than the cohesive energy for Cs metal, 18.54 kcal/mol. The authors suggested that the deposited Cs forms a disordered, uniform overlayer at low Cs coverage, and our observations support this model. The XPD peak positions and their intensities from the Cs/MoS_2 surface after the first 3 min of Cs evaporation, which are almost identical to those from a clean MoS_2 (Figure 4), demonstrate neither that the evaporation of Cs has formed any ordered overlayer nor that the Cs adsorption has induced short-range reconstruction of the substrate. Moreover, the absence of such Cs-induced relaxation certainly excludes the possibility of the Cs intercalation previously observed in the Li/MoS_2 system.[28,29] A greater intensity attenuation of both the S 2p and the Mo $3d_{5/2}$ core electrons at higher polar angle was observed, consistent with the screening effect of a uniform Cs overlayer on the MoS_2(0002) surface, given that the intensity

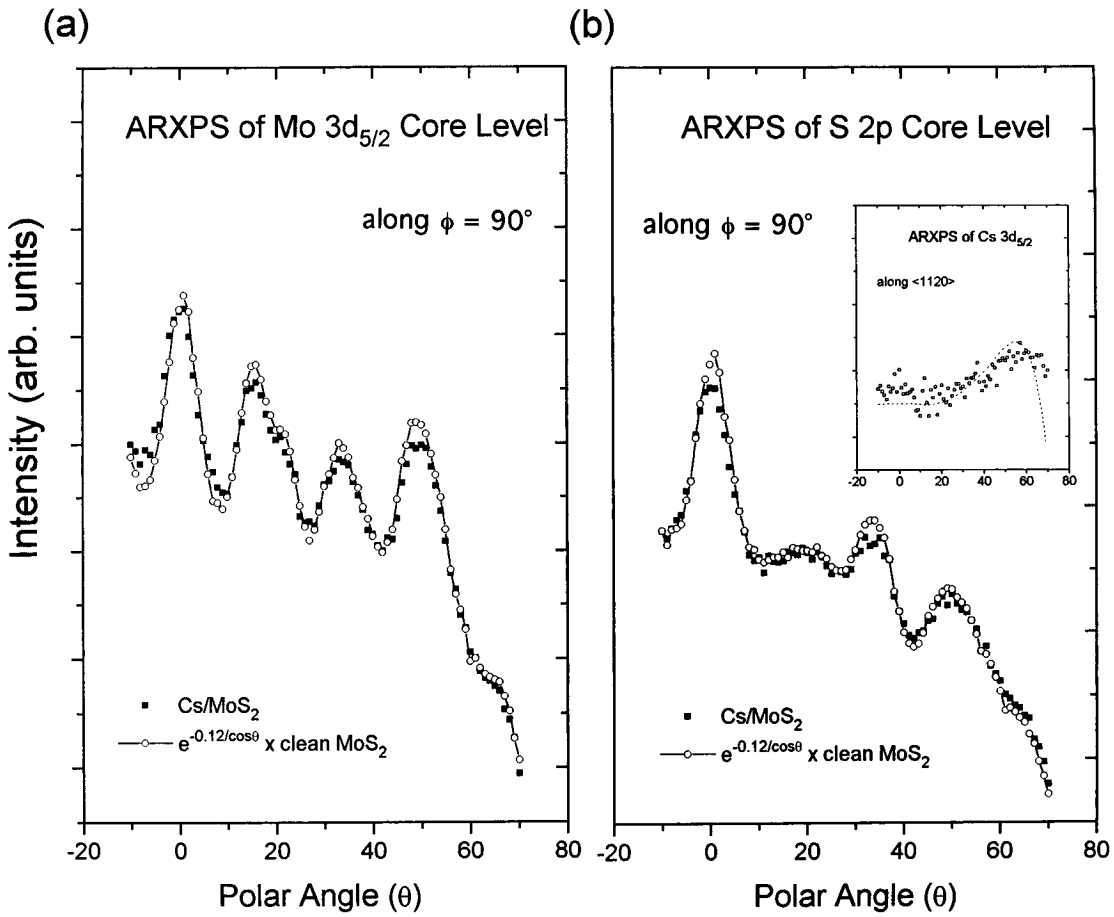

Figure 8. Comparison between the polar angle scan from clean MoS_2(0002) and Cs/MoS_2(0002) after the former was multiplied by the exponentially attenuating factor $\exp(-t/\lambda \cos\theta)$ with $t/\lambda = 0.12$, for both (a) Mo $3d_{5/2}$ and (b) S 2p core levels. The inset also shows comparison between ARXPS data of the Cs $3d_{5/2}$ core level and a theoretical intensity profile for the Cs 3d photoelectrons.

of photoelectrons traveling the distance L attenuates exponentially according to $\exp(-L/\lambda)$. Here, the inelastic electron mean free path λ depends upon the kinetic energy as well as the material in which the electrons travel. In Cs/MoS_2, the distance which the photoelectrons from the substrate travel through the Cs overlayer is equal to $t/\cos\theta$, where t is the nominal thickness of the Cs overlayer and θ the polar angle of emission direction from the surface normal. Then it is expected that the intensity of both core levels from the MoS_2 crystal will decrease as $\exp(-t/\lambda \cos\theta)$ due to the additional screening layer of Cs adatoms as θ increases. The XPD patterns of the Mo $3d_{5/2}$ and the S 2p core levels from the clean MoS_2(0002) were multiplied by the same exponential decay factor with the value for $t/\lambda = 0.12$. The resulting XPD patterns of both core levels were found to be essentially identical to those obtained after the Cs evaporation (Figure 8a,b). Using the experimentally measured value 13.5 + 4 Å for the core electrons,[30] the nominal thickness of the Cs overlayer after 3 min Cs evaporation is estimated to be *ca* 1.6 Å, corresponding to 0.31 ML (1 ML = $4.5 \times 10^{14}/\text{cm}^2$). Similarly, a simple model accounting for the angle dependence of the photoelectron intensity from the Cs overlayer due to inelastic scattering (Appendix) was compared with the ARXPS data of the Cs $3d_{5/2}$ core level (the inset of Figure 8b). The observed angle dependence of the Cs $3d_{5/2}$ core level photoemission is best described with the value $t/\lambda = 0.24$, which yields roughly 7 Å for the inelastic electron mean free path at $E = 786$ eV.

Conclusion

The ARXPS for a single-crystal MoS_2(0002) and the Cs-adsorbed MoS_2(0002) surface has been used to characterize the surface atomic structure. The intensity anisotropy of the Mo $3d_{5/2}$ and S 2p core level photoemissions shows forward scattering intensity maxima along the directions of nearest neighbors. Because of the finite electron escape depth and the short-range order of the scattered photoelectrons, the azimuthal scans of the Mo 3d and the S 2p levels exhibit 3-fold rotational symmetry of the MoS_2(0002) surface due to local trigonal prismatic structure, while the LEED and STM depict only the 6-fold symmetry of the top sulfur layers. Furthermore, we observed a difference in the XPD between the Mo and S core levels, which results from the inequivalent emitter sites that the Mo and S atoms occupy. The Cs deposition at room temperature did not result in any long-range-ordered structure. The XPD patterns of the substrate signals after the Cs adsorption indicate that the Cs overlayer has no preferred, local structure but provide evidence that the Cs submonolayer (0.31 ML) is spread and tightly bounded to the MoS_2 basal plane.

Acknowledgment. The authors thank A. Miller for allocation of time and services during the experiment in the SCIENTA ESCA laboratory. This work was supported by Department of Energy Grant No. DE-FG02-86ER13580.

Appendix: Angle Dependence of Photoelectron Intensity from a Thin Layer

In the direction θ, intensity I_w from a point located at z is

$$I_w = I_0 e^{-w/\lambda_s} e^{-w/\lambda} \qquad \text{(A-1)}$$

where λ and λ_s are the inelastic mean free paths in the material of the emitting layer and of the screening layer, respectively

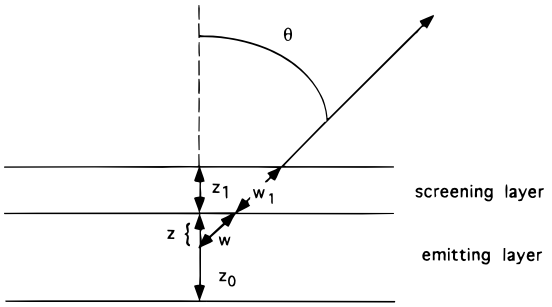

Figure 9. Schematic diagram of experimental geometry in ARXPS for angle dependence of photoelectron intensity due to inelastic scattering in a flat sample used to derive eq A-2.

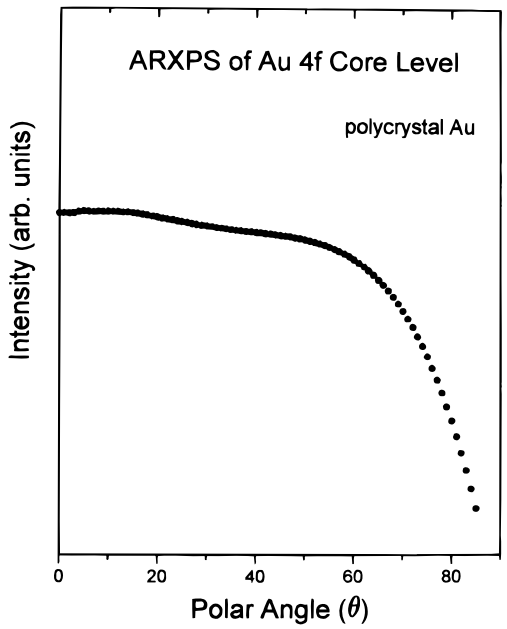

Figure 10. ARXPS experiment using clean polycrystalline Au of thickness 0.5 mm. The θ dependence of Au 4f level intensities is $R(\theta)$ according to eq A-2. Similar results for $R(\theta)$ were obtained from other reference systems including clean polycrystalline Pd (ref 32) and polystyrene ($\geq$300 Å) on Si as well as a monolayer of self-assembled calixarene membrane ($\approx$17 Å) on Au.

(Figure 9). I_0 can be rewritten as $n\sigma\lambda$, where n is the volume concentration of emitters in any given layer and σ is the photoemission cross section. Using eq A-1, integrate I_w for a given angle θ over all escape paths w's, $w = z/\cos\theta$, between the limits $w = 0$ and $w_0 = z_0/\cos\theta$

$$I_{\text{inel}}(\theta) = I_0 R(\theta) \int_0^{z_0/\cos\theta} e^{-w_s/\lambda_s} e^{-w/\lambda} dw$$

$$= I_0 e^{-z_s/(\lambda_s \cos\theta)} \lambda R(\theta)[1 - e^{-z_0/(\lambda \cos\theta)}] \quad \text{(A-2)}$$

where $R(\theta)$ is the directional variation of the photoelectron detection efficiency, or the so-called instrument response function. Euation A-2 is a "master" equation describing the θ dependence of photoelectron intensity from various types of samples. For an infinitely thick clean substrate ($z_0 \rightarrow \infty$, $z_s = 0$), eq A-2 becomes $I_{\text{inel}}(\theta) \propto I_0\lambda R(\theta)$, a flat intensity profile modified by the experimental detector efficiency. On the other hand, for a thin emitting layer of thickness z_0, the exponential factor in the brackets of eq A-2 can be expanded to yield $I_0 z_0 R(\theta)/\cos\theta$, roughly a $1/\cos\theta$ dependence since in a typical ARXPS $z_0/(\lambda \cos\theta)$ is less than unity.

The exact expression for $R(\theta)$ is, in general, instrument-specific and a complex function of many experimental parameters, i.e. the photoelectron energy, the transmission function of the analyzer, etc.[31] Nevertheless, the angle dependence of clean reference systems can yield an empirical way to assess the angle dependence of the instrument response function through eq A-1. In fact, a number of ARXPS experiments performed on various clean reference systems consistently have shown a general trend of more or less constant photoelectron detection up to a large angle, where it sharply decreases (Figure 10). This instrument response function was also included in the simulation of ARXPS of the Cs $3d_{5/2}$ core level.

References and Notes

(1) Pecoraro, T. A.; Chianelli, R. R. *J. Catal.* **1981**, *67*, 430.

(2) Kinkade, N. E. Eur. Pat. Appl. 84116467.6 and 84116468.4 (Dec. 28, 1984); assigned to Union Carbide Corporation.

(3) Santiesteban, J. G. Ph. D. Thesis, Lehigh University, 1988.

(4) Curtis, C. W.; Cahela, D. R. *Energy Fuels* **1989**, *3*, 168.

(5) Santiesteban, J. G.; Bogdan, C. E.; Herman, R. G.; Klier, K. *Proceedings of the 9th International Congress of Catalysis*, Calgary, 1988; North-Holland Publishing Co.: Amsterdam, 1988; p 561.

(6) Youchang, X.; Naasz, B. M.; Somorjai, G. A. *Appl. Catal.* **1986**, *27*, 233.

(7) Dianis, W. P. *Appl. Catal.* **1987,** *30*, 99.

(8) Murchison, C. B.; Conway, M. M.; Stevens, R. R.; Quarderer, G. J. *Proceedings of the 9th International Congress of Catalysis*, Calgary, 1988; North-Holland Publishing Co.: Amsterdam, 1988; p 626.

(9) Papageogopoulos, C. A. *Surf. Sci.* **1978**, *75*, 17.

(10) Kennou, S.; Ladas, S.; Papageogopoulos, C. A. *Surf. Sci.* **1984**, *152/153*, 1213.

(11) Karolewski, M. A.; Cavell, R. G. *Surf. Sci.* **1989**, *219*, 249.

(12) Karolewski, M. A.; Cavell, R. G. *Surf. Sci.* **1989**, *219*, 261.

(13) Egelhoff Jr., W. F. *CRC Crit. Rev. Solid State Mater. Sci.* **1990**, *16*, 213 and references therein.

(14) Fadley, C. S. In *Synchrotron Radiation Research Advances in Surface and Interface Science*; Bachrach, R. Z., Ed.; Plenum: New York, 1990.

(15) Fink, M.; Ingram, J. *At. Data* **1972**, *4*, 129. Gregory, D.; Fink, M. *At. Data Nucl. Data Tables* **1972**, *14*, 39.

(16) Richards-Babb, M. Ph. D. Thesis, Lehigh University, 1993.

(17) SCIENTA ESCA-300 User's Manual, Scienta, Uppsala, or alternatively one can get a general overview of the spectrometer from *High Resolution XPS of Organic Polymers The Scienta ESCA300 Database*; Beamson, G., Briggs, D., Eds.; John Wiley & Sons: Chichester, 1992; pp 3−8.

(18) Succi, M.; Canino, R.; Ferrario, B. *Vacuum* **1985**, *35*, 579.

(19) Su, C. Y.; Lindau, I.; Chye, P. W.; Oh, S.-J.; Spicer, W. E. *J. Electron Spectrosc. Relat. Phenom.* **1983**, *31*, 221.

(20) *Handbook of X-ray Photoelectron Spectroscopy*; Chastain, J., Ed.; Perkin-Elmer Co.: Minnesota, 1992.

(21) The atomic scattering factor for sulfur was interpolated from the calculated atomic scattering factors of phosphorus and chlorine in ref 15.

(22) Seah, M. P.; Dench, W. A. *Surf. Int. Anal.* **1979**, *1*, 2.

(23) Tong, S. Y.; Poon, H. C.; Snider, D. R. *Phys. Rev. B* **1985**, *32*, 2096.

(24) Kaduwela, A. P.; Herman, G. S.; Friedman, D. J.; Fadley, C. S. *Phys. Scr.* **1990**, *41*, 948.

(25) Stupian, G. W.; Leung, M. S. *Appl. Phys. Lett.* **1987**, *19*, 1560.

(26) Heckl, W. M.; Ohnesorge, F.; Binnig, G.; Specht, M.; Hashmi, M. *J. Vac. Sci. Technol.* **1991**, *B9*, 1072.

(27) Park, K. T.; Richards-Babb, M.; Hess, J. S.; Weiss, J.; Klier, K. Unpublished.

(28) Imanishi, N.; Toyoda, M.; Takeda, Y. *Solid State Ionics* **1992**, *58*, 333.

(29) Papageogopoulos, C. A.; Jaegermann, W. *Surf. Sci.* **1995**, *338*, 83.

(30) Fraser, W. A.; Florio, J. V.; Delgass, W. N.; Robertson, W. D. *Surf. Sci.* **1973**, *36*, 661.

(31) *Practical Surface Analysis*; Briggs, D., Seah, M. P., Eds.; John Wiley & Sons: Chichester, 1983.

(32) Gürer, E.; Klier, K. *Phys. Rev. B* **1992**, *46*, 4884.

JP9605865